The anatomy of the Gunn laser

S. Chung and N. Balkan

Related Articles

High beta lasing in micropillar cavities with adiabatic layer design
Appl. Phys. Lett. 102, 052114 (2013)

Portable optical-resolution photoacoustic microscopy with a pulsed laser diode excitation
Appl. Phys. Lett. 102, 053704 (2013)

Electro-optical and lasing properties of hybrid quantum dot/quantum well material system for reconfigurable photonic devices
Appl. Phys. Lett. 102, 053110 (2013)

Laser emissions from one-dimensional photonic crystal rings on silicon-dioxide
Appl. Phys. Lett. 102, 051103 (2013)

High-brightness tapered quantum cascade lasers
Appl. Phys. Lett. 102, 053503 (2013)

Additional information on J. Appl. Phys.

The anatomy of the Gunn laser

S. Chung[1] and N. Balkan[2,a)]

[1]*Department of Nano-Optics, Korea Polytechnic University, 2121 Jeongwang-dong, Shiheung City, Gyeonggi-do 429-793, Republic of Korea*

[2]*Department of Computing and Electronic Systems Engineering, University of Essex, Colchester CO4 3SQ, United Kingdom*

A monopolar GaAs Fabry–Pérot cavity laser based on the Gunn effect is studied both experimentally and theoretically. The light emission occurs via the band-to-band recombination of impact-ionized excess carriers in the propagating space-charge (Gunn) domains. Electroluminescence spectrum from the cleaved end-facet emission of devices with $Ga_{1-x}Al_xAs$ ($x=0.32$) waveguides shows clearly a preferential mode at a wavelength around 840 nm at $T=95$ K. The threshold laser gain is assessed by using an impact ionization coefficient resulting from excess carriers inside the high-field domain. © *2008 American Institute of Physics.* [DOI: 10.1063/1.2977719]

I. INTRODUCTION

We have shown recently that light is emitted from active region of a GaAs Gunn diode due to band-to-band recombination of impact-ionized carriers created by the high electric field in the propagating space-charge domains.[1] We also reported the correlation between the spontaneous emission intensity and the device length[2] and predicted that the spontaneous emission may evolve into stimulated emission when it is placed in a Fabry–Pérot (FP) cavity.[3]

In this paper we present our results of the current density–electric field (J-F) and electroluminescence (EL) intensity–electric field (L-F) characteristics together with the EL spectra of stimulated emission from the Gunn device. We also present the theoretical analysis and Monte Carlo simulation of the light emission mechanism invoking a combination of well-established physical phenomena, including the drift velocity saturation, impact ionization, and population inversion in GaAs.

II. EXPERIMENTAL

The waveguided sample used in the studies had a *n*-type GaAs active layer sandwiched between $Al_xGa_{1-x}As/GaAs$ ($x=0.32$) wave-guiding layers. The GaAs active layer had a carrier concentration of $n=4.8 \times 10^{17}$ cm^{-3} and a layer thickness of 1 μm. The wave-guiding layers and device structure together with contact configuration are shown in Figs. 1(a) and 1(b). The modified dumb-bell pattern shown in Fig. 1(b) was developed during our studies to provide emission facets without the introduction of loss regions that may occur as a result of contact diffusion in a conventional two terminal device.

Voltage pulses of duration ranging between 85 and 105 ns with a duty cycle less than 0.015% were applied along the device. The applied electric field was deduced from the voltage drop, taking into account aspect ratio of active region as described in Sec. III, between electrodes of the sample di-

vided by its length. The current flow through the device was determined by measuring the voltage across a 50 Ω resistor placed in series with the device. The light emitted from the sample was collected by an antireflective lens and dispersed using a 1/3 m monochromator (Bentham, M 300EA, 830 grooves/mm) which was fitted with bilateral straight slits, the width of which was variable between 10 μm and 8 mm. The spectra were detected using a cooled GaAs photomultiplier (Hamamatsu, R1767). The data were averaged and captured using a digital oscilloscope (Tektronix, TDS2012) with a bandwidth of 100 MHz.

III. RESULTS

In order to determine correctly the threshold field for negative differential resistance (NDR) aspect ratio of the ac-
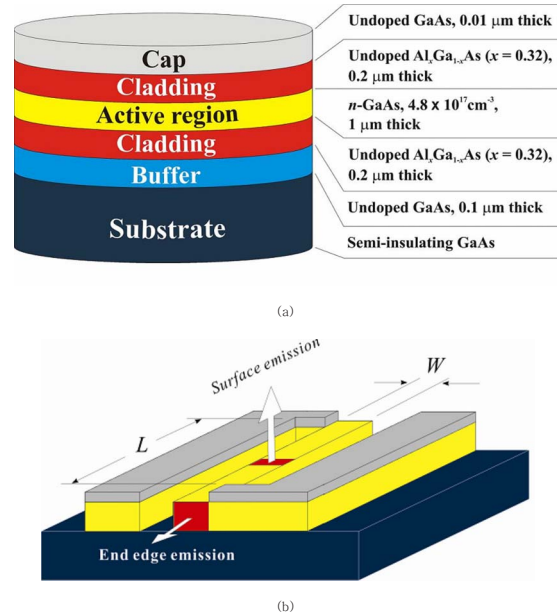

FIG. 1. (Color online) Wafer structure and device geometry of Gunn-effect laser; (a) waveguided structure and (b) FP device. The in-plane and vertical arrows in (a) indicate end-edge emission and top-surface emission, respectively.

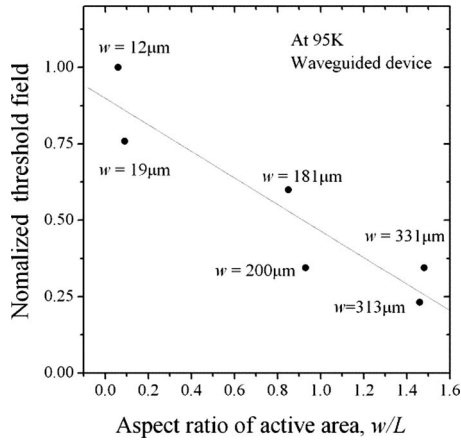a)Electronic addresses: htubalkan@essex.ac.ukut and balkan@essex.ac.uk.

FIG. 2. Dependence of normalized threshold electric field on device aspect ratios in a waveguided FP Gunn device measured at $T=95$ K. All samples have the same length of $L=200$ μm.

FIG. 3. Current density–electric field (J-F) and luminescence–electric field (L-F) curves at $T=95$ K. J-F and L-F were denoted with the symbol ● and ○, respectively.

tive region w/L should be taken into account. This is because the electric field calculated from the voltage drop along the active layer may be different from the true value for large aspect ratios. Assuming the uniform electric field along the conduction channel, the general expression for resistance is given by[4]

$$R = \frac{L}{|\sigma|S} = \frac{L}{|\sigma|wt} = \frac{1}{|\sigma|rt},\tag{1}$$

where the cross-sectional area of active layer is $S = w \times t$ with the width w and the thickness t. σ is the medium conductivity and r is the aspect ratio of active area defined by $r = w/L$.

While the thickness and the conductivity are constant, the aspect ratio depends on the external dimensions of the sample. The large aspect ratio provides the wider conduction channel for current flow and thus gives rise to small resistance across the area from Eq. (1) and a nonuniform electric field distribution between two electrodes. The experimental relation between the aspect ratio of active area and the normalized threshold field for a fixed device length of 200 μm is shown in Fig. 2. The data points, indicating threshold fields normalized to the one for $w=12$ μm, were fitted with the least-squares method.[5] Threshold fields measured from all the samples are normalized with the guideline in Fig. 2.

Figure 3 shows current density and light output power versus electric field characteristic of a FP Gunn laser measured at $T=95$ K with the fixed width of voltage pulse. Light emission from an end-edge facet increases abruptly above at the threshold $F_i=3.7$ kV/cm. Current density–electric field characteristic shows a slight preference for superlinear behavior as electric field is increased. The somewhat rapid increase in current density above at 3.2 kV/cm is indicative of current increase due to impact-ionized carriers produced by high-field domains forming as a result of NDR.[6]

Figure 4 shows end-facet EL emission spectra of the Gunn laser measured at $T=95$ K just above the NDR threshold field. It is worth noting that the prolonged application of higher electric field progressively degrades the device performance. Therefore for spectral measurements we used electric fields only slightly above the emission threshold. Figures
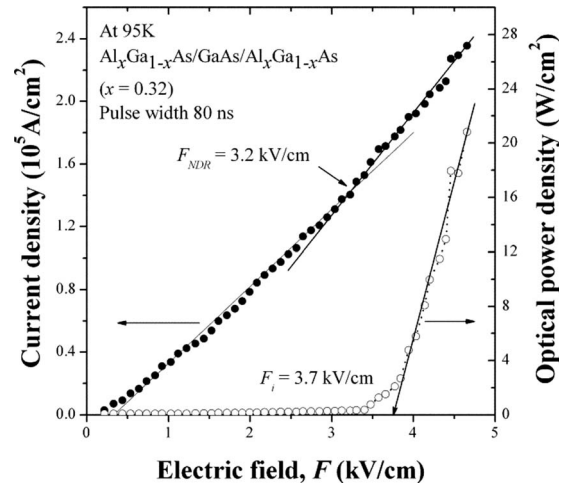
4(a)–4(c) show the emission spectra for 85, 95, and 105 ns wide applied voltage pulses, respectively. The spectra shown in Fig. 4(a) consist of a set of peaks, each of which has a family of lobes. This feature indicates the emergence of spectral modes by interference effect associated with the reflection of radiation at the faces of FP etalon.[7] We can see lasing from the device in Figs. 4(b) and 4(c). For the wider pulse of 95 ns, an emission mode at 844 nm appears with a half-width of 0.98 nm. In a conventional p-n junction FP laser, once the pumping energy well exceeds the threshold, multiple modes satisfying the phase condition appear accompanying main mode.[8] Similarly here, the spectrum of Gunn device observed for the pulse width of 105 ns does include multiple modes as depicted in Fig. 4(c), where the central dominant mode has a half-width of 0.75 nm. It is noted from Fig. 4 that the material gain linearly increases with the pulse
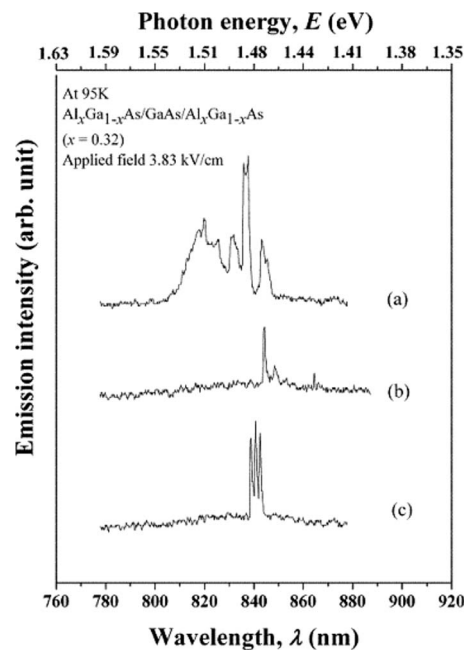

FIG. 4. EL spectrum of FP Gunn device at $F=3.83$ kV/cm with pulse widths of (a) 85 ns, (b) 95 ns, and (c) 105 ns.

TABLE I. Bulk GaAs material parameters used int he calculations.

Parameter	Value	Unit
Density, ρ[a]	5.3176	g/cm^3
Velocity of sound, s[b]	5.24×10^5	cm/s
High frequency dielectric constant at $T=300\ K$ and 95 K[c] $\varepsilon_\infty = 10.6(1 + 9 \times 10^{-5}T)$	10.8862/10.6906	–
Static dielectric constant, at $T=300\ K$ and 95 K[c] $\varepsilon_\infty = 12.4(1 + 1.2 \times 10^{-4}T)$	12.8464/12.5414	–
Polar optical phonon frequency, ω_0[c]	5.211×10^{13}	rad·s^{-1}
Equivalent intervally phonon frequency, ω_e[c]	4.4058×10^{13}	rad·s^{-1}
Non-equivalent intervally phonon frequency, ω_η[c]	4.2235×10^{13}	rad·s^{-1}
Acoustic deformation potential in central Γ valley, D_{ac}[c]	7	eV
Acoustic deformation potential in satellite L valley, D_{as}[c]	9.2	eV
Equivalent intervalley coupling constant, $D_{e,L\text{-}L}$[d]	10	eV/cm
Non-equivalent intervalley coupling constant, $D_{n,\Gamma\text{-}L}$[d]	10	eV/cm
Central valley effective mass, m_c^* ($m_0 = 9.1095 \times 10^{-31}$ kg)[e]	$0.067 m_0$	kg
Satellite valley effective mass, m_s^* ($m_0 = 9.1095 \times 10^{-31}$ kg)[e]	$0.35 m_0$	kg
Number of equivalent $L(111)$ valleys[f]	4	–

[a]O. Madelung, *Semiconductors-Basic Data*, 2nd ed. (Springer, Berlin, 1996), p. 104.
[b]O. Madelung, *Semiconductors-Basic Data*, 2nd ed. (Springer, Berlin, 1996), p. 108.
[c]M. A. Littlejohn, J. R. Hauser, and T. H. Glisson, 48(11), p. 4587 (1977).
[d]S. Adachi, *GaAs and Related Materias: Bulk Semiconducting and Superlattice Properties* (World Scientific, Singapore, 19940.
[e]A. D. Boardman, *Physics Program* (John Wiley & Sons, Chichester, 1980), p. 355–410.
[f]S. M. Sze, *Physics and Semiconductor Devices* (John Wiley & Sons, New York, 1981), p. 647.

width at the fixed voltage, indicative of the good controllability of the pulse width on gain relating to light emission. It is because the impact-ionized excess carrier density in a Gunn device is proportional to the transit number of the domain, which, in turn, is defined by the voltage pulse width. Hence the impact-ionized carrier density and the corresponding gain can be effectively controlled by a pulse width. In contrast, the applied field gives rise to the significant increases in the gain even with small amount over a NDR threshold. This might lead rightly to device degradation. The disadvantage of electric field operation is due to surgical current increase by considerable impact ionization made by multiple domains. Once the carrier multiplication process starts the current increases rapidly and the control over the device is lost leading to the destruction of the device due to excessive Joule heating.

IV. THEORETICAL MODEL

A. Electron transport model by Monte Carlo technique (Ref. 9)

In order to determine theoretically the onset of light emission, hence the NDR threshold, electron transport characteristics at high electric fields in GaAs were investigated using a Monte Carlo technique that took into account of the ionized-impurity and phonon scatterings in the parabolic Γ and L valleys.[1] The phonon scattering mechanisms permitted in the simulation are acoustic, optical, equivalent intervalley (EI), and nonequivalent intervalley (NEI). Simulation processes are described as follows.

Range and parameters. The simulation is accomplished in the range of electric fields between 0 and 10 kV/cm. The proper convergence of data is achieved by giving 2000 as the number of a real scattering events and using 100 V/cm as an electric field interval. Phonon energies and phonon occupation ratios for optical, EI, and NEI scattering are deduced from the respective phonon frequencies given in Table I.

Calculation. In a central valley, the rates of each scattering event can be estimated by using the proper equations given by Casey and Panish.[8] All the phonon scattering rates are calculated with the meshed energies (E) involving phonon energy changes, i.e., $E + \hbar\omega$ for phonon absorption and $E - \hbar\omega$ for phonon emission. Ionized impurity scattering does not invoke an energy loss since it is an elastic scattering. Hence the given meshed energy E is taken into account for the scattering.

Initialization. It is assumed that an electron drift along the k_z axis in the (k_ρ, k_z) coordinate k space, where k_ρ represents the sum of k_x and k_y vectors, remains fixed during an electron flight. The simulation is commenced with an arbitrary initial electron energy and position in k space. The arbitrary position does not have an influence on the final electron position if a number of drift events are occurred subsequently.

Selection process. The drift of an electron is terminated by a "scattering channel selection" process. The scattering channel selection is carried out by comparing a number generated randomly by the program with the normalized scattering rates. The comparison procedures are made with intravalley and, then, intervalley scatterings in order. The rate of the first intravalley scattering, i.e., ionized-impurity scattering, λ_1 is produced by being normalized with the total scat-
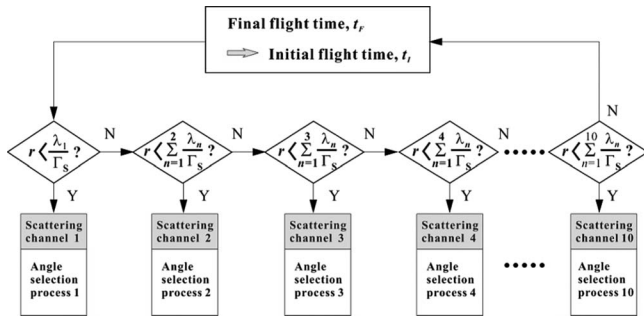
FIG. 5. Scattering channel selection processes for a real scattering process.

FIG. 6. Drift velocity-electric field curve of n-GaAs involving the phonon scattering process only.

tering rate Γ_s so that the normalized value λ_1/Γ_s becomes less than 1 comparable to a random number r. If the normalized value is smaller than r the ionized-impurity scattering rate is immediately added onto the next rate of scattering, i.e., optical phonon scattering. In the summation normalized with Γ_s, λ_2/Γ_s is used for the same comparison process. The compared scattering channels are indexed with the denotation of n as the following order: $n=1$ for the ionized-impurity scattering, $n=2$ and 3 for the emission and absorption of an optical phonon scattering, $n=4$ for an acoustic phonon scattering, $n=5$ and 6 for the emission and absorption of an equivalent intervalley phonon scattering, $n=7$ and 8 for the emission and absorption of nonequivalent $\Gamma \rightarrow L$ intervalley phonons, and $n=9$ and 10 for the emission and absorption of nonequivalent $L \rightarrow \Gamma$ intervalley phonons. If the process succeeds in finding a proper scattering channel by the selection rule as mentioned before it exits readily from the routine to calculate a final electron position in $\mathbf{k}$ space as shown in Fig. 5. Otherwise the process is regarded as a self-scattering process and the drift time is added on the initial drift time of the next run. When the number of real scattering events is satisfied at the given times the scattering processes will be terminated for the electric field. Then, the same process is initiated for the next electric field, etc.

Plotting. The energy and position changes in the scattered electron are accumulated and recorded for each electric field. Electron velocity change in k space can be expressed by differentiating the energy with k vector as

$$\mathbf{v} = \frac{1}{\hbar} \nabla_{\mathbf{k}} E(\mathbf{k}) = \frac{\hbar \mathbf{k}}{m^*}. \tag{2}$$

Therefore, a mean drift velocity, taking into account for all drift from starting position k_{zi} to final position k_{zf}, is defined as

$$v = \frac{\dfrac{\hbar}{m^*} \sum \displaystyle\int_{k_{zi}}^{k_{zf}} k_z dk_z}{\sum \displaystyle\int_{k_{zi}}^{k_{zf}} dk_z}. \tag{3}$$

The simulation result fitted with the sixth ordered polynomial curve at 300 K is shown in Figs. 6 and 7. The difference between the two figures shows the influence of impurity scattering on the drift velocity characteristics. Namely, the inclusion of impurity scattering reduces the low-field mobility and hence the drift velocity at the NDR threshold field. In fact,
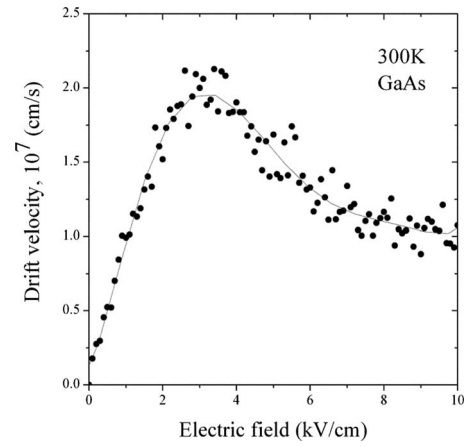
the impurity scattering dominates over electron-electron scattering at the low electric field range around the NDR threshold field.[10]

V. DOMAIN ELECTRIC FIELD

Figure 8 shows the spatiotemporal EL intensity measured from the top surface of a modified dumb-bell shape device with $L \times W = 600 \times 150$ μm^2 shown in Fig. 1(b). The measurements were carried out at $T = 300$ K with a fixed applied electric field of $F = 3.1$ kV/cm and pulse width of $t_{pulse} = 80$ ns. The light emission from the device was collected by a cleaved Franck-Condon/parity conserving type single mode optical fiber with a 9 μm inner core diameter. The traveling time, i.e., domain transit time, was calculated with a sample length and a domain velocity $v_d = 1.4 \times 10^7$ cm/s at NDR threshold shown in Fig. 7. The light intensity was measured from the device surface as a function of the propagating distance of the traveling domain from the cathode. The light intensity increases linearly during the domain transit. Higher light intensity corresponding to higher excess carrier density is created by impact ionization through the traveling domain field. A time-dependent potential of the high-field domain is[11]
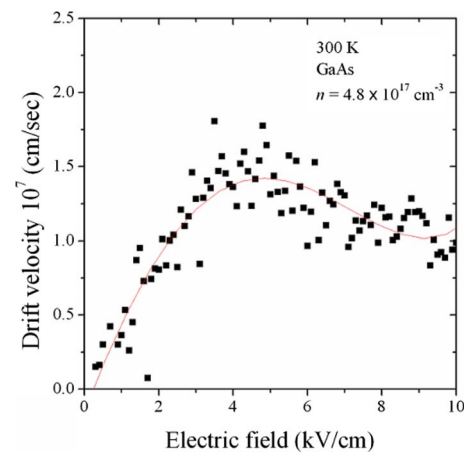
FIG. 7. (Color online) Drift velocity–electric field curve of n-GaAs involving both phonon scattering and impurity scattering.
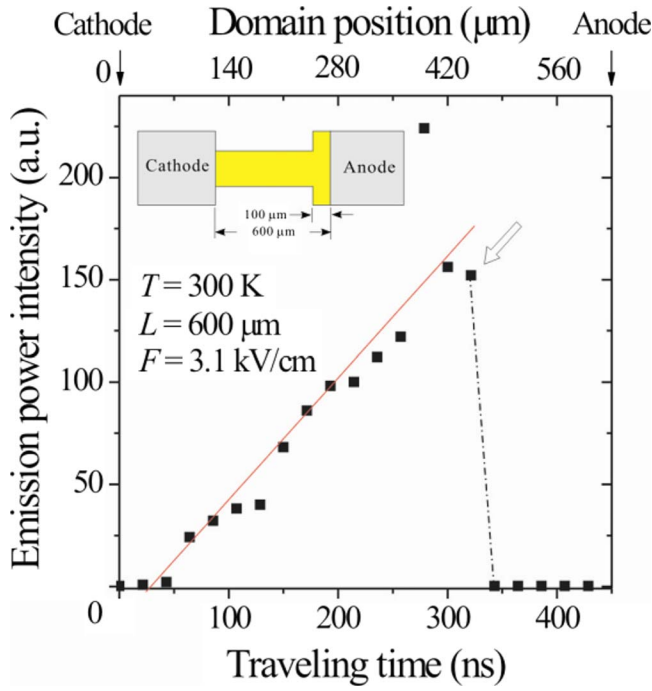
FIG. 8. (Color online) Spatiotemporal dynamics of a Gunn device with longitudinal length of 600 μm. The solid and dot lines indicate the best linear fit for the data from 0 to 430 μm (marked by a bold arrow) and the guideline for those from 430 to 600 μm, respectively.

$$\frac{dV_D}{dt} \cong \int_{F_R}^{F_d} [v(F_R) - v(F)]dF, \qquad (4)$$

where V_D is the domain potential. For the steady state, $dV_D/dt = 0$ and Eq. (4) satisfies the "equal areas rule,"[12] where two closed regions made by electron drift velocity-applied field (solid line) and domain drift velocity-domain field (dashed-dotted line) curves are equal in Fig. 9(a). When the current due to the applied field is increased from zero to the NDR threshold, the high-field domain is nucleated and continues to grow at an ever-increasing rate because electron velocity outside the domain $v(F_R)$ does not decrease owing to the constant current injection while domain velocity $v(F_d)$ is retarded by randomly distributed local imperfection in the semiconductor. It results in the change in time-dependent domain potential, i.e., $dV_D/dt \neq 0$ in Eq. (4). Therefore when electric fields above the NDR threshold are applied to the Gunn device, a propagating domain across the device will grow in the domain field as shown in Fig. 8 and the equal areas rule is not valid anymore because of the area inequality between two regions. We use Eq. (4) to define the "unequal areas rule." The electric field in the depletion region (depletion field) is[13]

$$F_{dep} = \frac{en_0 x}{\varepsilon}, \qquad (5)$$

where F_{dep} is the depletion field. With the assumption of quite a small diffusion coefficient, the accumulation layer has a finite thickness and electric field inside, F_{acc}. Maximum domain electric field satisfies $F_{dep} = F_{acc}$ at the interface between the accumulation layer and the depletion region. Therefore the relation is given by
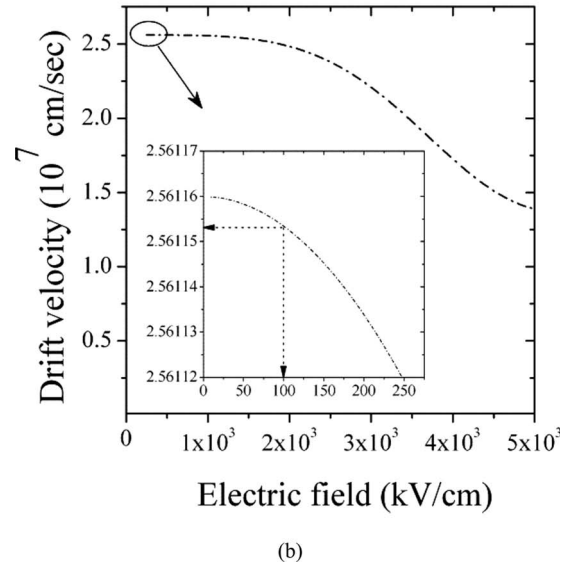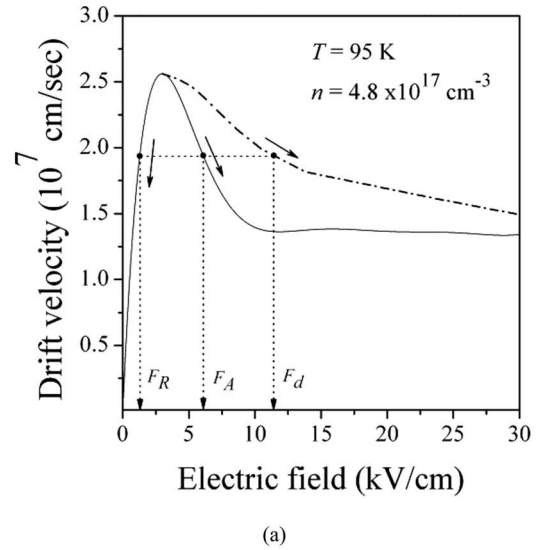

(a)

(b)

FIG. 9. Electric-field-dependent domain field curves drawn by (a) equal areas rule and (b) unequal areas rule at $T=95$ K. The solid and dashed-dotted lines of (a) indicates a drift velocity–electric field outside the domain produced by Monte Carlo technique and a drift velocity–electric field inside the domain, respectively. F_R, F_A, and F_d indicate electric field outside the domain, applied electric field, and electric field inside the domain. The inset of (b) shows the magnified view of domain fields near NDR threshold field, $F=3$ kV/cm. For an example, the arrows in the inset of (b) indicate the domain field ($F_d=100$ kV/cm) and the corresponding drift velocity (v_d =2.561 153×10⁷ cm/s).

$$\frac{en_{acc}d_{acc}}{\varepsilon} = \frac{en_0 d_{dep}}{\varepsilon}, \qquad (6)$$

where d_{dep} and d_{acc} are the thicknesses of depletion region and accumulation layer, respectively. n_{acc} is the electron density in the accumulation layer. Integration over the thickness including accumulation and depletion region produces domain potential difference V_d as

$$V_d = \frac{en_0 d_{dep}^2}{2\varepsilon}, \qquad (7)$$

where the thickness of the accumulation layer d_{acc} is negligible compared to that of the depletion region d_{dep}, and thus,

$d_{acc} + d_{dep} \approx d_{dep}$. Thus the electric field difference $F_d - F_R$ between the domain field and the field outside the domain is given by a single differentiation as

$$F_d - F_R = \frac{e n_0 d_{dep}}{\varepsilon}. \qquad (8)$$

Substituting Eq. (8) into Eq. (7),

$$V_d = \frac{(F_d - F_R)^2 \varepsilon}{2 e n_0}. \qquad (9)$$

The domain potential is actually the difference between a bias potential and the device potential in the rest of domain and thus is given by

$$V_d = V_b - F_R l, \qquad (10)$$

where V_b is the applied voltage and l is the device length. Substituting Eq. (10) into Eq. (9),

$$F_d - F_R = \left[(V_b - F_R l) \frac{2 e n_0}{\varepsilon} \right]^{1/2}. \qquad (11)$$

The dashed-dotted line of Fig. 9(a) shows the low temperature ($T = 95$ K) electric-field-dependent domain field curves of GaAs ($n = 4.8 \times 10^{17}$ cm^{-3}) drawn by equal areas rule, which describes a stable high-field domain. The maximum drift velocity is $v_d = 2.561\,16 \times 10^7$ cm/s at $F = 3.1$ kV/cm. As the applied electric field (F_A) is increased the electric field inside the domain (F_d) increased along the guideline drawn by the equal areas rule (dashed-dotted) and the electric field outside the domain (F_R) decreased. The primary curve in Fig. 9(b) was drawn by unequal areas rule, i.e., Eq. (11), which describes an unstable high-field domain. As the drift velocity reaches to the maximum value, $v_d = 2.561\,16 \times 10^7$ cm/s the domain field estimated by unequal areas rule increases rapidly and readily exceeds over $F_d \approx 100$ kV/cm, which is the onset of impact ionization. Therefore the unequal areas rule is more appropriate for explaining light emission of the Gunn device due to impact ionization.

VI. IMPACT IONIZATION COEFFICIENT

The relationship between light emission intensity and impact ionization coefficient is straightforward as shown by others.[14,15] Lucky-drift theory[16] gives an analytic expression for the ionization coefficient, α.

In the simple parabolic bands,

$$\alpha \lambda = \frac{1}{x} \left\{ e^{-x} + \left(\frac{e^{-2rx^2} - e^{-x}}{1 - 2rx} \right) \right. $$
$$\left. + P_T \left[e^{-x(1-\zeta)} + \left(\frac{e^{-2rx^2(1-\zeta)} - e^{-x(1-\zeta)}}{1 - 2rx} \right) \right] \right\}, \qquad (12)$$

where x is a ratio of effective energy loss per collision to ionization threshold energy $x = E_i / eF\lambda$. E_i is the threshold energy for ionization, F is the applied field, and λ is the scattering mean free path. P_T is $P_T = 1 - \exp[-2rx(x-3)]$ for $x \geq 3$ and ζ is $\zeta = P_T / 2rx^2$. For a better fit to the experimental data a simple multiplicative factor γ is introduced to Eq. (12) as[17]
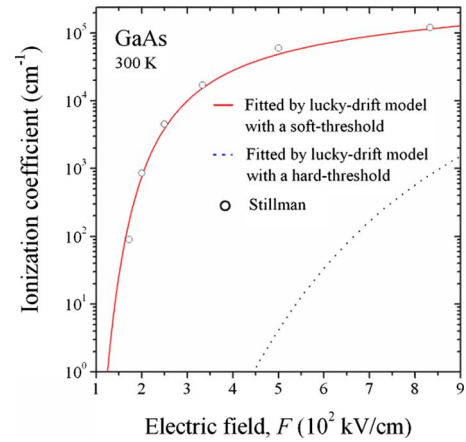

FIG. 10. (Color online) Impact ionization coefficients for electron in GaAs at 300 K. The open circles indicate experimental data suggested by Singh (Ref. 18) and the solid line is the theoretical curve of a lucky-drift model with a soft threshold [Eq. (13)] and the dotted line is the same curve with a hard threshold [Eq. (12)].

$$\alpha \lambda = \frac{\gamma}{x(1-\eta)} \left[e^{-x(1-\eta)} + \left(\frac{e^{-2rx^2(1-\eta)} - e^{-x(1-\eta)}}{1 - 2rx} \right) \right]$$
$$+ \frac{\gamma P_T}{x} \left[e^{-x(1-\zeta)} + \left(\frac{e^{-2rx^2(1-\zeta)} - e^{-x(1-\zeta)}}{1 - 2rx} \right) \right], \qquad (13)$$

where $\eta = E_0 / E_i$ with the injection energy E_0.

Using Eq. (13), we fitted the experimental data by Singh[18] in Fig. 10. We used the following parameters: the phonon occupation number $n_{phonon} = 0.483$, the ratio of effective energy loss per collision to threshold energy $r = 0.009\,38$, the mean free path $\lambda = 40$ Å, and the simple multiplicative fitting factor $\gamma = 0.12$. It is noted that a threshold field for impact ionization is $F_{th} = 125$ kV/cm where the number of electron-hole pairs generated by an electron per unit traveling distance, i.e., ionization coefficient, is a unity.

VII. EXCESS CARRIER DENSITY

In order to evaluate the decay and multiplication rate of excess carriers and to find the lasing threshold carrier density, we need to determine the multiplication factor and recombination rate in a Gunn device. With a prior assumption of no change in ionization rate during a domain transit, the excess carrier density n_{ex} is given by[19]

$$n_{ex} = \int_0^L n_0(x) \alpha_e dx, \qquad (14)$$

where n_0, α_e, and L are the background electron density, ionization coefficient, and the device length, respectively. For a device operated by a pulse width longer than the domain transit time, a multiplicative factor γ, representing a multiplication term of the domain repetition rate (f_T) and the pulse width (t_{pulse}), should be taken into account with a carrier loss rate of $\exp(-t_{tr}/\tau_r)$. Then n_{ex} is given as

$$n_{ex} = n_0 \alpha_e L \gamma \exp(-t_{tr}/\tau_r), \qquad (15)$$

where t_{tr} is the domain transit time and τ_r is the radiative recombination time. To avoid unnecessary complexity with

TABLE II. Input parameters for the calculation of impact-ionized excess carrier density at $T=95$ K

Device length L (μm)	Transit frequency $f_T=v_d/L$ (Hz)	Pulse duration t_{pulse} (nsec)	Domain transit time, $t_{\text{tr}}=1/f_T$ (sec)	Recombination Lifetime, τ_{tr} (nsec)
200	1.3×10^9	105	7.7×10^{-10}	0.5

excess carrier dependent-recombination time we employ the recombination time defined under the fixed excess carrier density $n_{\text{ex}}=n_0$. The bulk recombination rate U depends non-linearly on the excess carrier density,[20]

$$U = A(n - n_0) + B(pn - p_0 n_0) + C_p(p^2 n - p_0^2 n_0) + C_n(pn^2 - p_0 n_0^2), \quad (16)$$

where $n=n_0+n_{\text{ex}}$ and $p=p_0+p_{\text{ex}}$. n_0 and p_0 indicate the background electron and hole densities, respectively. If we assume that $n_{\text{ex}}=p_{\text{ex}}$, Eq. (16) can be simplified to

$$U \approx An_{\text{ex}} + B(p_0+n_0+n_{\text{ex}})n_{\text{ex}} + C_p(p_0^2+2p_0 n_{\text{ex}}+n_{\text{ex}}^2)n_{\text{ex}} + C_n(n_0^2+2n_0 n_{\text{ex}}+n_{\text{ex}}^2)n_{\text{ex}}. \quad (17)$$

The recombination lifetime is defined as

$$\tau_r = n_{\text{ex}}/U. \quad (18)$$

From Eqs. (17) and (18), τ becomes

$$\tau_r \approx [A + B(p_0+n_0+n_{\text{ex}}) + C_p(p_0^2+2p_0 n_{\text{ex}}+n_{\text{ex}}^2) + C_n(n_0^2+2n_0 n_{\text{ex}}+n_{\text{ex}}^2)]^{-1}. \quad (19)$$

The second term, indicating the radiative recombination lifetime, is[21]

$$\tau_r = [B(p_0+n_0+n_{\text{ex}})]^{-1}, \quad (20)$$

where the radiative recombination coefficient B is $B=2.1\times10^{-9}$ cm^3/s (Ref. 22) and the background electron density n_0 is $n_0=4.8\times10^{17}$ cm^{-3}. The intrinsic hole density p_0 in n-type doped semiconductor is negligibly small compared to n_0. For simplicity, we assumed that the excess electron density n_{ex} is equal to n_0. Therefore the radiative recombination lifetime at 95 K is calculated to $\tau_r=5\times10^{-10}$ s. Using Eq. (15) and the input parameters as in Table II, we can now evaluate the excess carrier density for a 200 μm long Gunn device at different pulse widths. The domain field is assumed with a value somewhat larger than a threshold impact ionization field, $F_d=130$ kV/cm, where the ionization coefficient corresponds to $\alpha_e=2.5$ cm^{-1}. Dependence of excess carrier density on a pulse width is shown in Fig. 11.

VIII. LASER GAIN (REF. 23)

Using Fermi's golden rule,[24] laser gain obtained from the net stimulated emission between energy levels 1 and 2, g_{21}, is given,

$$g_{21} = \frac{\pi e^2 \hbar}{nc\varepsilon_0 m_0^2} \frac{1}{h\nu_{21}} |M_T(E_{21})|^2 \rho_r(E_{21}-E_g)(f_2-f_1), \quad (21)$$

where n is the index of refraction in GaAs, c is the speed of light in free space, ε_0 is the free space permittivity, m_0 is the

free electron mass, e is the electron charge, and $h\nu_{21}$ is the emitted photon energy during the transition from the energy E_2 to E_1. $M_T(E_{21})$ is the transition matrix element of bulk GaAs. $\rho_r(E)$ represents the reduced density of states function defined as[25]

$$\rho_r(E) = \frac{\rho(k)}{dE(k)/dk}, \quad (22)$$

where $\rho(k)$ is $\rho(k)=k^2/2\pi^2$ and the denominator $dE(k)/dk$ is equal to $\hbar^2 k/m_r$ with a reduced mass m_r. f_1 and f_2 are the occupation probability as defined using Fermi statistics under nonequilibrium conditions. These are given for the valence band and conduction band as

$$f_1 = \frac{1}{\exp[(E_1-E_{F_v})/kT]+1}, \quad (23a)$$

$$f_2 = \frac{1}{\exp[(E_2-E_{F_c})/kT]+1}, \quad (23b)$$

where E_{F_v} and E_{F_c} are quasi-Fermi levels in the valence band and conduction band, respectively. The Padé approximation provides an analytic expression for the excess electron density- and temperature-dependent quasi-Fermi level $E_{F_c}(n_{\text{ex}},T)$ for the conduction band as[26]

$$E_{F_c}(n_{\text{ex}},T) = (\ln n_{\text{ex}} + K_1 \ln(K_2 n_{\text{ex}}+1) + K_3 n_{\text{ex}})kT, \quad (24)$$

where the constants $K_1=4.896\,685\,1$, $K2=0.044\,964\,57$, and $K3=0.133\,376\,0$. The remaining terms have their usual meanings.
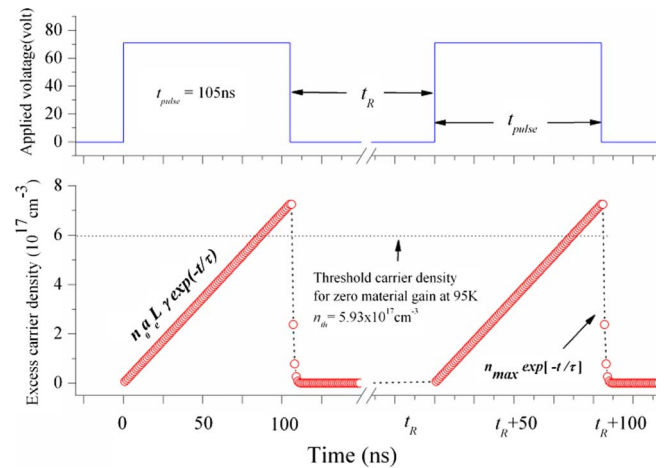

FIG. 11. (Color online) Dependence of excess carrier density on pulse width 200 μm long Gunn device. T_R indicates the pulse repetition rate and t_{pulse} is the pulse duration. n_{max} is the excess carrier density in the end of the pulse. The ionization coefficient is $\alpha_e=2.5$ cm^{-1}. Other denotations are quoted from Eq. (15). The horizontal dash line indicates the excess carrier density for zero material gain, $n_{\text{ex}} \approx 6\times10^{17}$ cm^{-3}.
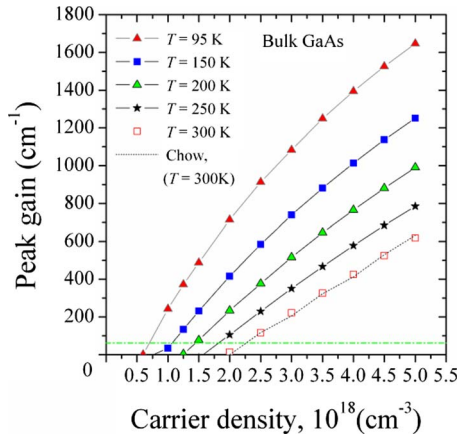
FIG. 12. (Color online) Peak material gain of GaAs as a function of carrier density at different temperatures. The dashed-dotted line indicates the lasing threshold gain, $\langle g \rangle_{th} = 67$ cm^{-1}.
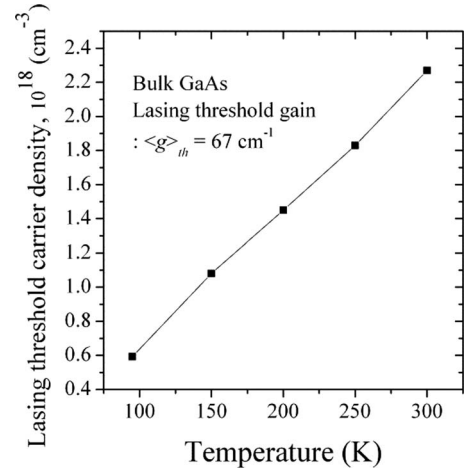

FIG. 13. Threshold lasing carrier density of GaAs as a function of temperature. The lasing threshold carrier density was determined at the lasing threshold gain.

The charge neutrality condition ($n=p$) can be used for the calculation of $E_{F_v}(p,T)$ in the valence band. E_1 of Eq. (23a) and E_2 of Eq. (23b) are defined with assumption of parabolic bands and the k-selection rule as

$$E_1 = E_v - (E_{21} - E_g)\frac{m_r}{m_v}, \tag{25a}$$

$$E_2 = E_c - (E_{21} - E_g)\frac{m_r}{m_c}. \tag{25b}$$

Taking into account energy uncertainty of the electron states causing energy broadening, optical gain is determined with integration over transitions contributing to the gain at the specific photon energy $E = h\upsilon_0$,

$$g(h\upsilon_0) = \int g_{max}(E_{21})(f_2 - f_1)L(h\upsilon_0 - E_{21})dE_{21}, \tag{26}$$

where $g_{max}(E_{cv})$ is the maximum material gain given in Eq. (21) and $L(h\upsilon_0 - E_{cv})$ is a Lorentzian lineshape function.

When losses in the cavity are taken into account the threshold gain required for the lasing condition, $\langle g \rangle_{th}$, can be obtained as follows:[27]

$$\Gamma\langle g \rangle_{th} = \alpha_i + (1/L)\ln(1/r_1 r_2), \tag{27}$$

where the average internal loss of a cavity is $\alpha_i \approx 10$ cm^{-1} and the mean mirror intensity reflection coefficient for GaAs-air interface is $R = r_1 r_2 \approx 0.32$. Taking the optical confinement $\Gamma = 1$ and the device length $L = 200$ μm, we find the lasing threshold gain $\Gamma\langle g \rangle_{th} = 67$ cm^{-1}.

The gain evaluated by Eq. (26) was degraded with increasing temperature at a given carrier density as shown in Fig. 12. At a lower temperature, the tail of the Fermi–Dirac distribution function becomes steeper, which results in the greater difference of $f_2 - f_1$, i.e., a more efficient population inversion distribution. The results agree well with the data by Chow et al.[26] at $T = 300$ K.

Figure 13 shows the lasing threshold carrier density as a function of temperature. The lasing threshold carrier densities for different temperatures are determined by the intercept between the material gain peak curve and the lasing thresh-

old gain line as shown in Fig. 12. It is clear from Fig. 13 that the threshold carrier density is linearly increased with increasing the temperature for bulk GaAs.

Figure 14 shows the low temperature ($T = 95$ K) peak material gain dependence on pulse width with the threshold field of impact ionization $F_{th} = 130$ kV/cm. As the pulse width is increased, the buildup of impact-ionized excess carriers in the active region of a device is enhanced to a level sufficient to achieve positive material gain (at $t_{pulse} = 88$ ns) and further lasing threshold (at $t_{pulse} = 105$ ns) as shown in Fig. 14.

IX. CONCLUSION

We investigated light emission from a Gunn device associated with impact ionization of traveling high-field domains and demonstrated lasing operation of a GaAs FP Gunn device with Al$_{1-xB}$Ga$_x$As ($x = 0.38$) waveguide structure. The lasing spectrum of the modified dumb-bell Gunn device is observed at an applied electric field of $F \geq 3.83$ kV/cm and pulse width of 95 ns. The peak optical power density at an
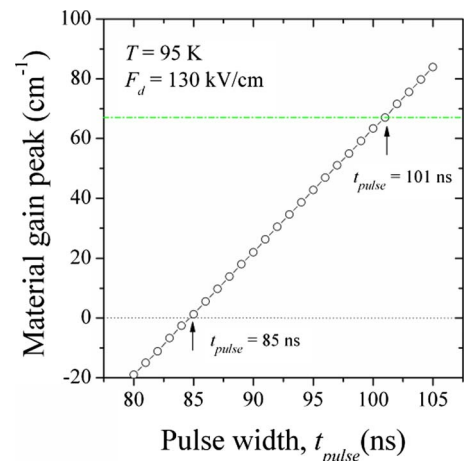

FIG. 14. (Color online) Peak gain as a function of pulse width $T = 95$ K. The horizontal upper (dash) and lower (solid) lines indicate the lasing threshold and zero material gain, respectively.

applied field of $F = 3.83$ kV/cm is around 13.5 W/cm^2 corresponding to an emitted power of $P = 25.4$ μW. Lasing from the Gunn device is due to band-to-band radiative recombination of impact-ionized carriers inside high-field domains. A theoretical assessment showed that a threshold excess carrier density for an inverted population distribution is correlated with an applied pulse width and electric field. A numerical and analytic quantitative account of a lasing model was given using the following procedure:

(1) obtain the electron drift velocity-electric field curve using the Monte Carlo method,
(2) obtain the maximum domain field from the unequal areas rule,
(3) obtain the ionization rate from the theoretical curve, defined by the lucky-drift model, fitting the experimental data,
(4) model the initial buildup of light emission taking into account the domain frequency, the accumulation effect of the additional excess carriers in the accumulation layer of the domain, and the spontaneous recombination rate in GaAs, and
(5) obtain the maximum material gain as a function of the applied pulse width by using the gain spectrum including a lineshape function.

ACKNOWLEDGMENTS

[1]J. S. Heeks, IEEE Trans. Electron Devices **13**, 68 (1966).
[2]N. Balkan and M. Hostut, Physica B (Amsterdam) **272**, 291 (1999).
[3]S. Chung, A. Boland-Thoms, J. Y. Wah, N. Balkan, and B. K. Ridley, Semicond. Sci. Technol. **19**, S400 (2004).
[4]W. H. Hayt, Jr., *Engineering Electromagnetics* (McGraw-Hill, New York, 1985), p. 136.
[5]E. Kreyszig, *Advanced Engineering Mathematics*, 6th ed. (Wiley, New York, 1981), p. 1029.
[6]B. K. Ridley, Semicond. Sci. Technol. **3**, 542 (1988).
[7]C. H. Gooch, *Gallium Arsenide Lasers* (Wiley, London, 1969), p. 104.
[8]H. C. Casey, Jr. and M. B. Panish, *Heterostructure Lasers* (Academic, New York, 1978), pp. 178–179.
[9]W. Fawcett, A. D. Boardman, and S. Swain, J. Phys. Chem. Solids **31**, 1963 (1970).
[10]H. D. Rees, J. Phys. Chem. Solids **30**, 643 (1969).
[11]H. L. Hartnagel, *Gunn-Effect Logic Devices*, 1st ed. (Heinemann Educational Books, London, 1973), p. 25.
[12]P. N. Butcher, W. Fawcett, and C. Hilsum, Br. J. Appl. Phys. **17**, 841 (1966).
[13]H. L. Hartnagel, *Gunn-Effect Logic Devices*, 1st ed. (Heinemann Educational Books, London, 1973), Chap. 2.
[14]N. Balkan, B. K. Ridley, and A. J. Vickers, *Negative Differential Resistance and Instabilities in 2-D semiconductors* (Plenum, New York, 1993), pp. 215–249.
[15]E. Zanoni, L. Vendrame, P. Pavan, M. Manfredi, S. Bigliardi, R. Malik, and C. Canali, Appl. Phys. Lett. **62**, 402 (1993).
[16]B. K. Ridley, J. Phys. C **16**, 3373 (1983).
[17]B. K. Ridley, J. Phys. C **16**, 4733 (1983).
[18]J. Singh, *Semiconductor Optoelectronics: Physics and Technology* (McGraw-Hill, Singapore, 1995), p. 147.
[19]P. P. Bohn and G. J. Herskowitz, IEEE Trans. Electron Devices **19**, 14 (1972).
[20]R. N. Hall, Proc. Inst. Electr. Eng. **106B**, 923 (1960).
[21]D. K. Schroder, *Semiconductor Material and Device Characterization* (Wiley, New York, 1990), p. 361.
[22]Y. P. Varshni, Phys. Status Solidi **19**, 459 (1967).
[23]L. A. Coldren and S. W. Corzine, *Diode Lasers and Photonic Integrated Circuits* (Wiley, New York, 1995), pp. 112–136.
[24]*Ibid*, p. 508, 1995.
[25]P. S. Zory, Jr., *Quantum Well Lasers* (Academic, San Diego, 1993), p. 34.
[26]W. W. Chow, S. W. Koch, and M. Sargent III, *Semiconductor-Laser Physics* (Springer-Verlag, Berlin, 1994), p. 47.
[27]L. A. Coldren and S. W. Corzine, *Diode Lasers and Photonic Integrated Circuits* (Wiley, New York, 1995), p. 39.